Physics of the Earth and Planetary Interiors 210–211 (2012) 1–7

Contents lists available at SciVerse ScienceDirect

Physics of the Earth and Planetary Interiors

journal homepage: www.elsevier.com/locate/pepi

A new *P*-velocity model for the Tethyan margin from a scaled *S*-velocity model and the inversion of *P*- and *PKP*-delay times

Sung-Joon Chang [a,*], Suzan Van der Lee [a], Megan P. Flanagan [b]

[a] Dept. of Earth and Planetary Sciences, Northwestern University, 1850 Campus Drive, Evanston, IL 60208-2150, USA
[b] Lawrence Livermore National Laboratory, P.O. Box 808, L-205, Livermore, CA 94551, USA

ARTICLE INFO

Article history:
Received 7 November 2011
Received in revised form 31 May 2012
Accepted 20 August 2012
Available online 31 August 2012
Edited by George Helffrich

Keywords:
P-velocity model
3D reference model
Tethyan margin
Seismic tomography
Empirical scaling

ABSTRACT

We estimate a 3D *P*-velocity model for the Tethyan margin by inverting *P*- and *PKP*-delay times. The inversion is relative to a 3D reference model, which is a scaled *S*-velocity model for the same region. This *S*-velocity model was derived by jointly inverting regional *S* and Rayleigh waveform fits, teleseismic arrival times, Rayleigh-wave group velocities, and independent Moho constraints. Thus, our 3D reference model includes structures resolved over a larger depth range as well as more information on aseismic regions with few stations than is typically obtained from traditional teleseismic delay time inversions. We then inverted *P*- and *PKP*-delay times to obtain perturbations relative to the scaled 3D reference model. Comparing our *P*-velocity model (EAPV11) with *P*-velocity models derived from *P* data only, we find a model with more uniform and better depth resolution, including velocity anomalies for aseismic regions with few stations such as North Africa, southeastern Arabia, and the East European platform. Using EAPV11 to predict arrival times for relatively accurately located events that were not used in the inversion shows that our model produces significant variance reductions for these data as well. Therefore, our approach to build *P*-velocity models based on 3D reference *S*-velocity models may provide a practical way to better estimate *P*-velocity anomalies in the uppermost mantle and beneath aseismic regions with few stations.

© 2012 Elsevier B.V. All rights reserved.

1. Introduction

In seismic tomography, three-dimensional (3D) *P*-velocity models for the mantle are typically derived from first-arriving *P* waves, particularly from teleseismic events. However, it is challenging for such data to obtain depth resolution in the crust and uppermost mantle because of their relatively steep wave paths at these depths. Moreover, the *P* data provide little ray path coverage beneath aseismic regions with few seismic stations. In attempts to deal with these challenges, regional *P*-arrival times and/or other phases such as *pP*, *pwP*, and *PP* have been included in seismic tomography (e.g., Spakman et al., 1988; Van der Hilst et al., 1997; Bijwaard et al., 1998). Finite frequency kernels (e.g., Montelli et al., 2004; Yang et al., 2006) have been utilized to sharpen imaged structures. 3D *S*-velocity models are generally better resolved in such regions, since they are typically derived from surface waves, which have better resolving power for layering in the lithosphere and asthenosphere, including for aseismic regions with few stations. Therefore, we incorporate information from an *S* wave model to enhance *P*-velocity models, such that our 3D *P*-velocity model is resolved more comprehensively than possible with *P* data alone.

To include *S* velocity model information into *P* velocity models, empirical scaling relations have been usually adopted to scale *S*-velocity anomalies relative to 1D reference *S* model to *P*-velocity perturbation relative to 1D reference *P* model using a scaling factor ($\delta \ln \beta / \delta \ln \alpha$), which is often depth invariant. Rawlinson and Fishwick (in press) used the *Vp*/*Vs* ratio from a 1D reference model to convert absolute *S* velocities to absolute *P* velocities. Ritzwoller et al. (2003) used laboratory measurements of the effects of composition and temperature on seismic velocity to convert *S*-velocity models to *P*-velocity models.

Here, we combine empirical scaling relations and an inversion of *P*- and *PKP*-delay times. First, we convert *S* velocity anomalies from a known model to 3D *P* velocity anomalies, using an empirical scaling relation. The *S* velocity model used was recently derived by Chang et al. (2010) from a joint inversion of regional waveform fits, teleseismic *S*- and *SKS*-arrival times, fundamental-mode Rayleigh-wave group velocities, and independent Moho constraints. Second, we create a 3D reference *P*-velocity model by adding the estimated *P* anomalies to 1D reference *P*-velocity model, *iasp91* (Kennett and Engdahl, 1991). Then, we invert *P*- and *PKP*-delay times relative to the 3D reference *P* velocity model. The intention of this two-step process is to construct a *P* velocity model that benefits on the

* Corresponding author. Address: School of Environmental Sciences, University of East Anglia, Norwich, Norfolk NR4 7TJ, UK.
E-mail addresses: sungjoon.chang@gmail.com, Sung-Joon.Chang@uea.ac.uk (S.-J. Chang).

0031-9201/$ - see front matter © 2012 Elsevier B.V. All rights reserved.
http://dx.doi.org/10.1016/j.pepi.2012.08.005

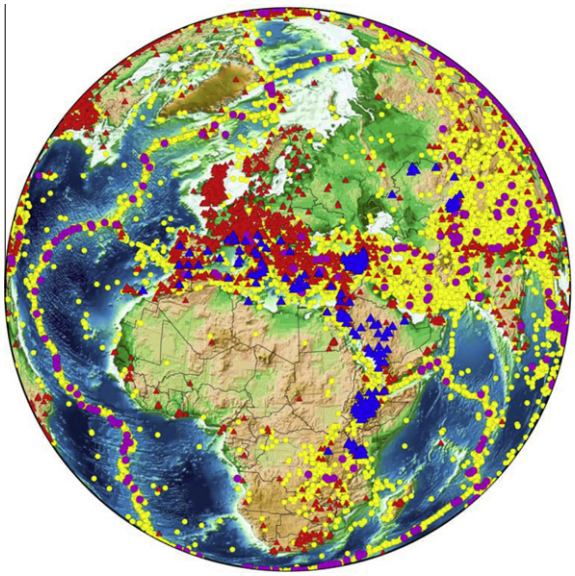

Fig. 1. Events and stations used for teleseismic *P*- and *PKP*-delay times. Purple circles and blue triangles represent events and stations used for relative delay time estimation with MCCC, respectively. Yellow circles and red triangles mean events and stations from the EHB database, respectively. (For interpretation of the references to color in this figure legend, the reader is referred to the web version of this article.)

one hand from information on the lithosphere and asthenosphere as well as aseismic regions provided predominantly by the *S*-velocity model and, on the other hand, from information on lateral variations in and deep *P* velocity structure provided by the inversion of *P*- and *PKP*-delay time data. We compare our newly derived *P*-velocity model (EAPV11) with previous *P*-velocity models and then present arrival time predictions from EAPV11 for the comparison with that from a 1D *P*-velocity model.

2. Method

Our model consists of the three-dimensional distribution of *P*-velocity anomalies and the two-dimensional distribution of Moho depth anomalies. The *P* velocity anomalies at various depths down to 1930 km and the Moho depth anomalies are parameterized using pentagonal and hexagonal pyramid basis functions located at grid points within a spherical shell. The grid points are the result of a triangular tessellation of the spherical shell (Wang and Dahlen, 1995), an approach first used in geoscience by Baumgardner and Frederickson (1985). The center of our grid is located at 35°N/22.5°E and the extent of the grid is approximately 70° in all directions. At the surface, two neighboring grid points (the corners of the triangles) are approximately 1° apart. The total number of grid points is just over half a million (16,541 per spherical shell for 32 *P*-velocity layers and 1 Moho layer). Only about two thirds of all grid points are significantly sampled by our data. The Moho depth parameters are not allowed to be updated during the inversion for *P*-velocity because of the poor resolving power of *P*-arrival times for Moho depth. The lateral variations in Moho depth in our model are those of the three-dimensional reference model, which is based on the *S*-velocity model of Chang et al. (2010), where extensive detail is provided on its inference.

To estimate the *P*-velocity distribution in three dimensions, the following *P*-delay time equation is usually inverted,

$$\mathbf{G}_\alpha \mathbf{m}_\alpha = \mathbf{d}_\alpha^0, \tag{1}$$

where $\mathbf{G}_\alpha$ is a sensitivity kernel matrix for *P*-delay times (for example, ray path segment lengths), $\mathbf{m}_\alpha$ is a vector of model parameters representing the *P*-velocity distribution, and $\mathbf{d}_\alpha^0$ is a data vector which is obtained by subtracting predicted arrival times through a 1D reference *P*-velocity model from observed arrival times:

$$\mathbf{d}_\alpha^0 = \mathbf{d}_\alpha - \mathbf{d}_\alpha^{1D}, \tag{2}$$

where $\mathbf{d}_\alpha^{1D}$ are the predictions through a 1D reference model, $\mathbf{d}_\alpha$ the observed arrival times, and $\mathbf{d}_\alpha^0$ the arrival time residuals, delay times.

Instead of a 1D reference model, we use a 3D reference *P*-velocity model, which is derived from a previously estimated 3D *S*-velocity model (Chang et al., 2010). This 3D reference model, hopefully closer to the true model than 1D reference models, may enable us to find a solution with use of iterative linearized inversion. The 3D reference model already reduces the total variance in our *P*- and *PKP*-delay times by 4% compared to 1D reference model *iasp91*. The derivation of this 3D reference *P* velocity models from the 3D *S* velocity model is motivated by the observation of Schmid et al. (2004), who found that *P* delay (δt_α) times scale roughly as 1/3 of *S* delay times (δt_β) for the Mediterranean part of the study region. Such scaling implies that *P* velocity anomalies ($\delta\alpha$) roughly equal *S*-velocity anomalies ($\delta\beta$) in units of m/s, because the reference *P* and *S* velocities (α, β) scale with a factor of $\sqrt{3}$ and the *S*/*P* delay time ratio is proportional the square of this factor $\left(\frac{\delta t_\beta}{\delta t_\alpha} \approx \frac{\alpha^2 \delta\beta}{\beta^2 \delta\alpha}\right)$. Our conversion thus starts by simply copying the velocity anomalies from Chang et al. (2010) *S*-velocity model to identical *P* velocity anomalies. However, to construct the 3D reference *P*-velocity model, these anomalies were added to 1D reference *P*-velocity model, *iasp91* (Kennett and Engdahl, 1991), rather than to a scaled, *P*-velocity version of the 1D reference *S*-velocity model MEAN (Marone et al., 2004) that was used by Chang et al. (2010), which includes a low-velocity zone in the uppermost mantle primarily because of its original application in the Mediterranean Sea region. This 1D model switch implies a depth-dependent scaling that takes into account that most of our *P* observations are made away from the low-velocity zone, and that the cause(s) (possibly water or partial melt) of the low *S*-velocity zone do not have the same effect on *P* velocities. This is based on the observation that the performance of MEAN in predicting *P*- and *PKP*-delay times is poorer than that of *iasp91* as well as the observation that high-velocity anomalies are obtained in the *P*- and *PKP*-delay time inversion for uppermost mantle regions where low-velocity anomalies exist in the 3D reference model.

The predicted times by the 1D model *iasp91* are already subtracted from the observed arrival times in Eq. (1). Now we use only the scaled 3D *P*-velocity anomaly model $\mathbf{m}_{\alpha'}$ to predict *P* delays $\mathbf{d}_{\alpha'}$ by

$$\mathbf{G}_\alpha \mathbf{m}_{\alpha'} = \mathbf{d}_{\alpha'}, \tag{3}$$

and subtract these predicted *P* delays $\mathbf{d}_{\alpha'}$ from the observed residuals $\mathbf{d}_\alpha^0$. Then, we invert

$$\mathbf{G}_\alpha \mathbf{m}_{\alpha''} = \mathbf{d}_{\alpha''}, \tag{4}$$

where $\mathbf{d}_{\alpha''} = \mathbf{d}_\alpha^0 - \mathbf{d}_{\alpha'}$. We calculate model $\mathbf{m}_{\alpha''}$ by solving this equation using the iterative conjugate-gradient algorithm LSQR (Paige and Saunders, 1982a,b). Therefore, our final 3D *P*-velocity model is defined as

$$\mathbf{m}_\alpha = \mathbf{m}_\alpha^{1D} + \mathbf{m}_{\alpha'} + \mathbf{m}_{\alpha''}, \tag{5}$$

where $\mathbf{m}_\alpha^{1D}$ is 1D reference *P*-velocity model *iasp91*, $\mathbf{m}_{\alpha'}$ is the scaled 3D *S*-velocity model of Chang et al. (2010), and $\mathbf{m}_{\alpha''}$ contains the *P* perturbations relative to this scaled 3D reference model from *P* and *PKP*-delay time inversion. Origin time and location uncertainties for events are considered in the inversion as in Chang et al.

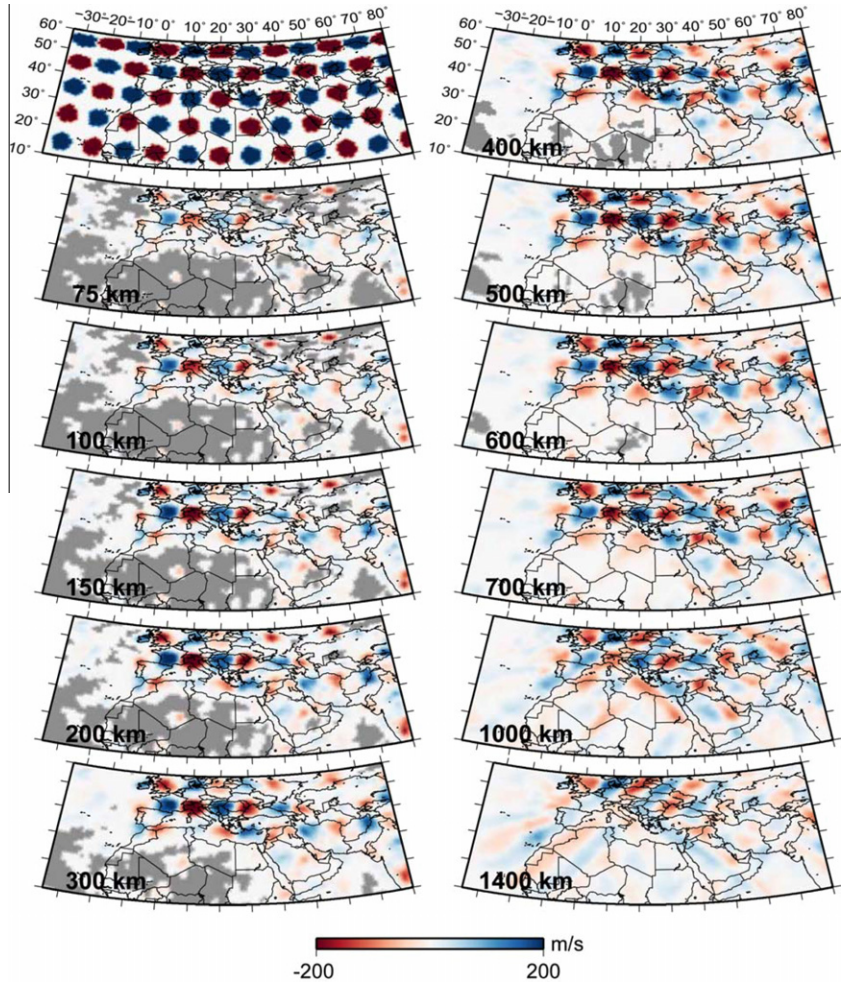

Fig. 2. Resolution tests with noise contamination. The horizontal slices of cylindrical *P*-velocity perturbations with radii of 3° in the true model and inversion results at various depths are presented. Regions not covered by *P*-arrival time data set are illustrated in gray.

(2010). Ray tracing is performed using the shooting method of VanDecar (1991). We corrected arrival times for topography and Earth's ellipticity prior to inversion.

3. Data

P- and *PKP*-phase arrival times are obtained from two sources. First, we use high-resolution relative arrival times of teleseismic *P* and *PKP* phases measured with multi-channel cross-correlation technique (MCCC; VanDecar and Crosson, 1990) in Ethiopia, Kenya, Saudi Arabia, and the Mediterranean region by Benoit et al. (2006), Park and Nyblade (2006), Park et al. (2007), and Schmid et al. (2004), respectively. Additionally, we measured *P* phase relative arrival times in Turkey and central Asia from seismograms from a PASSCAL experiment (Eastern Turkey Seismic Experiment), the Kyrgyz Seismic Telemetry Network (KNET), and the Kazakhstan Network (KZNET). The total number of *P*- and *PKP*-phase relative arrival times is around 10,300. Epicentral distance ranges from 30° to 90° for *P* phase and from 87° to 140° for *PKP* phase, respectively. We assign an uncertainty of 0.3 s to the relative arrival times, which is used to weigh this data's influence during the inversion.

Second, we use *P* phase arrival times from the reprocessed ISC database (EHB; Engdahl et al., 1998; E.R. Engdahl, personal communication, 2007) from 1964 to 2007. The number of *P* arrival times for our study region from the EHB database is around 3900,000. We discarded residuals greater than ±6 s, while more stringent criteria with cutoff of ±3–4 s are used in the previous *P*-velocity estimations (e.g., Ritzwoller et al., 2003; Koulakov et al., 2009). The epicentral range is from 14° to 95°. We did not include local and regional *P* arrival times from events with epicentral distances less than 14°, because for this range *Pn* phases obscure *P* phases, which make it difficult to pick phases accurately. Moreover, we currently adopt 1D ray tracing, which may cause severe errors in tracing *Pn* phases due to no consideration of Moho topography. We assign an uncertainty of 1.0 s to these *P* arrival times from the EHB database. Locations of stations and events for the two types of arrival times are shown in Fig. 1.

4. Resolution tests

In order to investigate the resolving power of *P* delays relative to the 3D reference model, we performed resolution tests with ±200 m/s cylindrical anomalies with radii of 3° (Fig. 2). We added Gaussian random noise to synthetic "data" with a standard deviation in proportion to the uncertainty of our data. The test results show poor resolution down to 300 km depth except for the European region, which implies that the adopted 3D reference model plays a critical role for the velocity estimation in other regions at these depths. As depth increases, resolution improves and spreads over a wider region. From 300 to 1000 km depth, fair resolution is obtained for the whole study region except for North Africa and oceans.

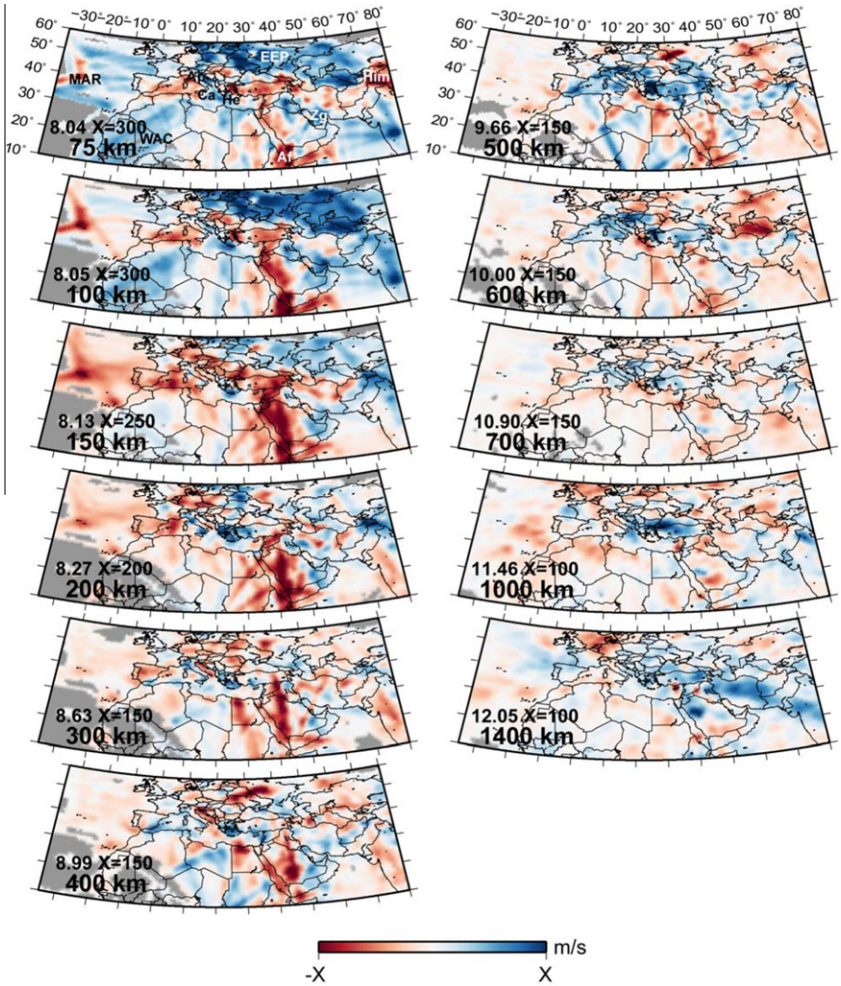

Fig. 3. EAPV11 at various depths. Velocity perturbations are relative to the reference model *iasp91* (Kennett and Engdahl, 1991). The reference *P* velocity at each depth is shown on the left side in km/s units. Regions not covered by data set are illustrated in gray. This gray region is based on the sensitivity of the 3D *S*-velocity model in the reference model. Af = Afar hotspot, AP = The Apennines, Ca = Calabrian arc, EEP = East European platform, He = Helenic arc, Him = Himalayas, MAR = mid-Atlantic ridge, WAC = West African craton, Zg = Zagros belt.

Therefore, *P* arrivals may adjust the velocity distribution of the 3D reference model for this depth range. Between 1000 and 1400 km, the polarity of anomalies is generally well resolved, although smearing occurs and anomaly strengths are underestimated.

5. Results and discussion

The use of a 3D reference *P*-velocity model reduces the total variance of the *P*- and *PKP*-delay time residuals by 4 % compared to using 1D reference model *iasp91*. The inversion of *P*- and *PKP*-delay times relative to this 3D reference model yields an additional variance reduction of 23%. We obtain about the same variance reduction of 23% if we invert the *P*- and *PKP*-delay times relative to 1D reference model *iasp91*, which is obviously less than the total variance reduction of 28% we obtain by inverting the data relative to the 3D reference model. This implies that 3D reference model allows us to sample the model space more extensively than possible with a 1D reference model.

Various depth slices from our *P*-velocity model (EAPV11) are shown in Fig. 3. For the lower mantle, where arrival time data dominate our results, EAPV11 looks similar to the *P*-velocity model of Bijwaard et al. (1998) derived with *P* data alone. However, for the upper mantle, where our 3D reference model affects the resulting *P*-velocity model, the two models are quite different. EAPV11 shows a low-velocity anomaly beneath the Himalayas at 75 km depth like other orogenic belts such as the Anatolian plateau, the Zagros belt, Hindu Kush, and Pamir. The mid-Atlantic ridge is clearly outlined as a narrow low-velocity zone down to at least 150 km depth. A very low-velocity anomaly in the uppermost mantle is observed beneath the Afar hotspot, which persists down to at least the transition zone. The West African craton and the East European platform, stable aseismic regions, are observed as high-velocity anomalies in EAPV11 at 75–150 km depths. These structures are mainly inherited from the 3D reference model, considering the poor *P* data resolution at these depths (Fig. 2). Wider slab fragments are observed beneath the Mediterranean and its surrounding region in the transition zone (500 km slice in Fig. 3) than Bijwaard et al.'s model, which is also found in the *P*-velocity model of Koulakov et al. (2009).

The difference between EAPV11 and the 3D reference model are presented in Fig. 4. These anomalies represent refinement by information on *P*-velocity structure from *P* and *PKP* delays with respect to 3D reference model. It seems that anomalies generally have reverse polarities to anomalies in EAPV11 down to 300 km depth, which implies that we shifted velocity anomalies in the correct positive direction when converting *S* anomalies to *P* anomalies, but also that the range of *P* anomalies is not as wide as that of *S*

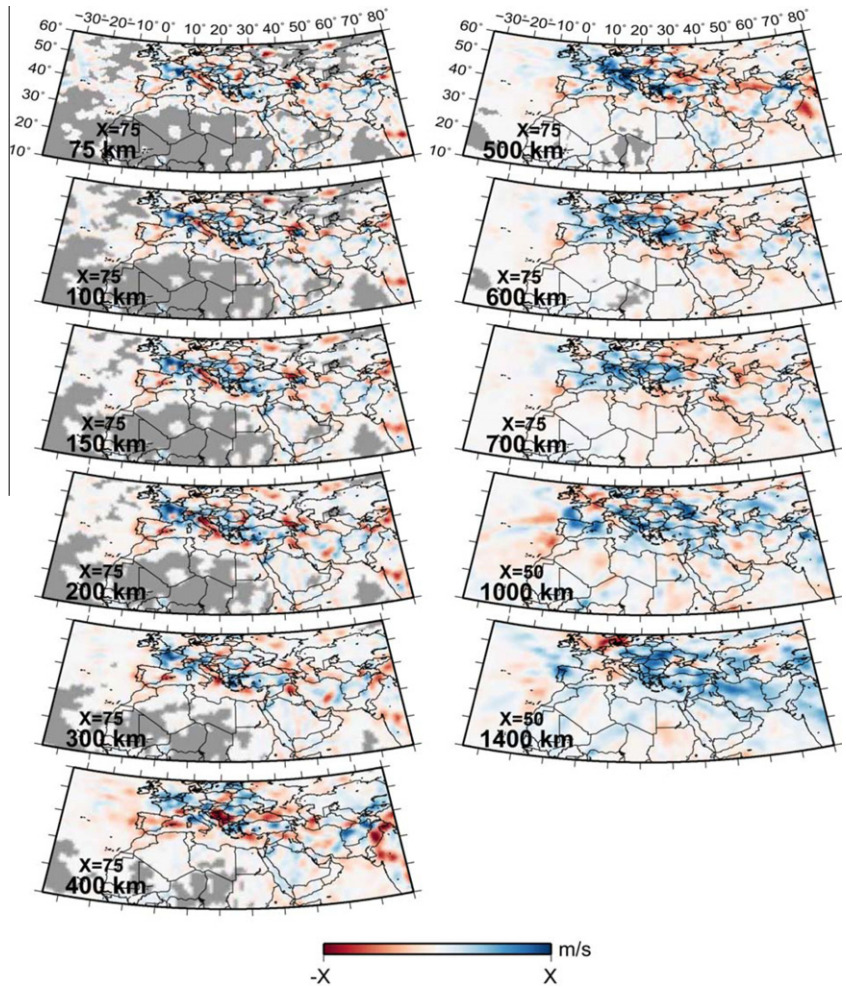

Fig. 4. *P*-velocity perturbations of EAPV11 relative to the 3D reference model. These perturbations are obtained through *P*- and *PKP*-delay time inversion. Regions not covered by the data set are illustrated in gray.

anomalies. This may indicate that low-velocity anomalies in the uppermost mantle are not entirely thermal in origin, but also affected by partial melt, water, or other compositional factors. On the other hand, the *P* data inversion enhanced anomalies from the transition zone to the lower mantle, especially for high-velocity anomalies representing subducting slabs. Upper mantle anomaly amplitudes are small compared to anomalies in EAPV11, but they become comparable to EAPV11 in the lower mantle, demonstrating considerable adjustments to the 3D reference model.

Some cross sections from EAPV11 are presented in Fig. 5. The Hellenic and Calabrian slabs are well resolved (Fig. 5a–b), and the Apenninic slab is detached at 100–200 km, showing the asthenospheric flow through the gap at 100–200 km by a low-velocity anomaly (Fig. 5c). Underneath the Zagros belt, a dipping slab is observed down to the transition zone, albeit with smearing, which is thought to be the Neo-Tethys oceanic lithosphere (Fig. 5d). These features are mostly inherited from the 3D reference model, because the *S*-velocity model by Chang et al. (2010) shows similar features and we have limited resolving power for these structures (Fig. 2). One noticeable difference from the 3D reference model is a distinct high-velocity anomaly within the transition zone beneath the Pannonian basin (Fig. 5c), which could represent a subducted slab from the Carpathians.

Although EAPV11 has an advantage because of its 3D reference model in containing information on aseismic regions with few stations, there is a possibility to deteriorate *P* travel time prediction since the information is mainly inherited from the scaled *S*-velocity model. To investigate the potential of EAPV11, as a model constructed by the combination of empirical scaling relation and an inversion of *P* and *PKP* delays, we performed first arrival time predictions with a 3D finite difference code (Flanagan et al., 2007) for comparison with a ground truth database (GT25: events that are located within 25 km with 95% confidence). The GT25 data set was not used in our inversion, so it tests the ability of EAPV11 to predict arrival times independently. We present arrival time residual histograms at station KHO in Fig. 6, which shows remarkable delay-time variance reductions of 39% for EAPV11 compared to *iasp91*. This means arrival times with EAPV11 are consistent with observed arrival times from GT25. This variance reduction is more than twice the 17% obtained by Flanagan et al. (2007) for the same station and GT25. We also presented arrival time residual surfaces (correction surfaces) for our 3D model in Fig. 6.

The bulk (37%) of the success of this correction surface is because of the 3D reference model. This is so because the GT25 data set consists of *Pg*, *Pn*, and *P* phases from epicenter to 40° which are critically influenced by the crust and uppermost mantle structure. This result might seem contrary to the variance reduction results of the *P* and *PKP* delays discussed above, where the 3D reference model reduces variance by only 4%, while delay-time inversion reduces the variance by 23%. This seems so because variance reduction in the *P* data set used in the inversion is achieved mostly

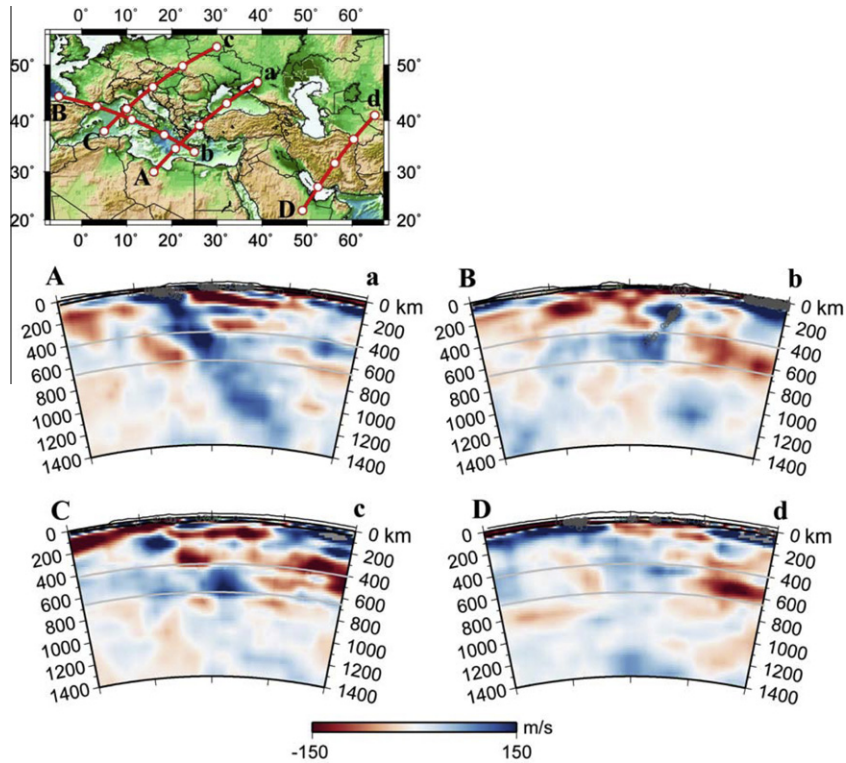

Fig. 5. Vertical cross-section maps beneath the Hellenic arc (a), beneath the Calabrian arc (b), beneath the northern Apennines (c), and perpendicular to the Zagros belt (d). Moho depth and surface topography are shown in black solid lines. Moho distributions in EAPV11 are derived from Chang et al. (2010). Topography is exaggerated 10 times. Dark gray open circles represent events, and light gray lines indicate 410 and 660 km discontinuities. Great-circle paths corresponding to cross sections are indicated on the top panel. White circles on the great-circle paths correspond to ticks shown in the cross sections.

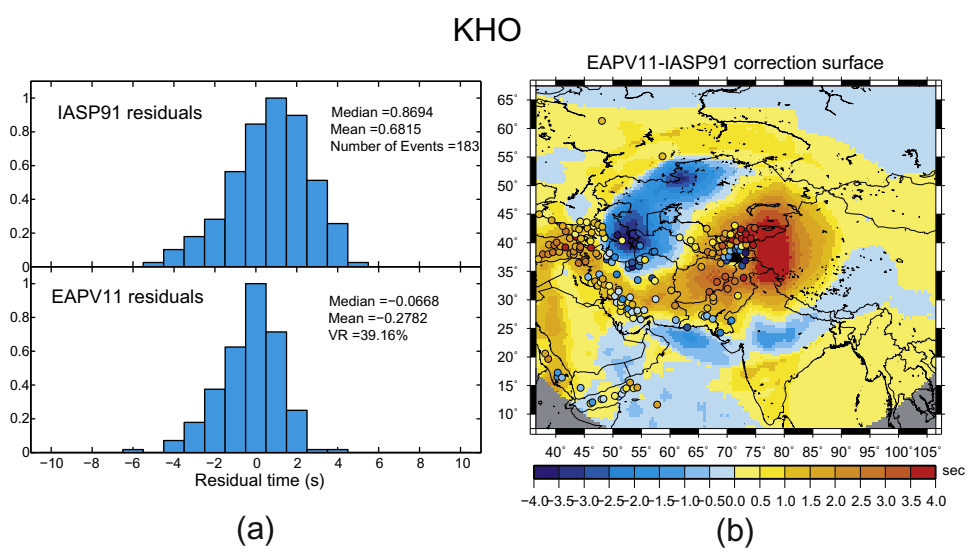

Fig. 6. Histograms of arrival time residuals for *iasp91* and EAPV11 models and arrival time residual surfaces at station KHO. (a) We used GT25 data set (uncertainty less than 25 km with 95 % confidence) to compare with predicted arrival times from velocity models. Arrival time residuals are estimated by GT25 – *iasp91* and GT25 – EAPV11, respectively. VR represents variance reduction. (b) Arrival time residual surface (EAPV11 – *iasp91*) is presented with locations of stations (black triangle) and event points from GT25 data set (GT25 – *iasp91*) with the same color scale. The surfaces were calculated from predicted arrival times with EAPV11 assuming sources are located at 10 km depth beneath each node. The GT25 events have focal depths of 0∼20 km.

through structure deeper than 300 km, while the regional GT25 data set is mostly sensitive to structure shallower than 300 km. The latter structure is largely inherited from the 3D reference model. The *P* data set used in the inversion is from events further than 14°, and is dominated by teleseismic delays. Rather than constraining shallow mantle structure with hard to pick *Pn* phases from local earthquakes, approximating its uncommon wave paths (Simmons et al., 2011), and with other phases such as *PP* and *Pp* phases (Bijwaard et al., 1998), we rely on shallow mantle structure that is inherited from a 3D *S* velocity model.

These empirically scaled anomalies inherited from the 3D reference model contribute constructively to the estimated *P* delay times, despite the simplifying approximations made for the scaling factor. EAPV11 thus shows a straightforward way to provide additional resolution in *P*-velocity models for aseismic regions with few stations, the crust, and the uppermost mantle. A complete set of arrival time predictions for stations in this region with several 3D *P*-velocity models will be performed in a subsequent study (Validation of regional travel time predictions along the Tethyan margin for three *P*-velocity models built with different approaches, In preparation).

6. Conclusions

Our new *P*-velocity model for the Tethyan margin is successfully derived from the inversion of *P*-and *PKP*-delay times with respect to a 3D reference model. The 3D reference model is derived from a 3D *S*-velocity model obtained by jointly inverting teleseismic *S*- and *SKS*-arrival times, regional *S*- and Rayleigh waveform fits, fundamental-mode Rayleigh-wave group velocities, and independent Moho constraints (Chang et al., 2010), assuming that *P* and *S* anomalies are similar. Resolution tests confirm that the *P*- and *PKP*-delay times update the *P*-velocity model from depths of about 300 to 1400 km, but the crustal and uppermost-mantle *P* velocities are predominantly inherited from the 3D reference model.

Our *P*-velocity model (EAPV11) shows major, well-known mantle structures such as the Hellenic slab as well as aseismic regions without stations such as the West African craton and the East European platform, which are hardly detected by *P* arrivals only because of a dearth of ray paths in these regions.

To investigate the validity of EAPV11, we performed first-arrival time predictions with GT25 data for station KHO, and we observed improved arrival time prediction with variance reduction of 39%, which is a dramatic increase compared to the 17% of Flanagan et al. (2007). Therefore, our methodology may show a way to provide resolution for aseismic regions with few stations, the crust, and the uppermost mantle, which has been challenging in traditional *P* delay time inversions.

Acknowledgments

We thank Margaret Benoit, Andy Nyblade, Yongcheol Park, and Christian Schmid for sharing their relative *P* arrival time data sets. We are also grateful to Bob Engdahl for access to his EHB database. Raiden Hasegawa, Ryan Lange, and Xiaoting Lou helped us to get relative arrival time data at central Asia and Turkey. We thank Stewart Fishwick and an anonymous reviewer for providing valuable suggestions that improved this manuscript. All figures were created using Generic Mapping Tools (GMT; Wessel and Smith, 1998). This work was supported by the Korea Research Foundation Grant KRF-2006-214-C00092 funded by the Korean Government (MOEHRD) and the U.S. DOE under contract DE-FC52-04NA25541.

References

Baumgardner, R.B., Frederickson, P.O., 1985. Icosahedral discretization of the two-sphere. SIAM J. Numer. Anal. 22, 1107–1115.
Benoit, M.H., Nyblade, A.A., VanDecar, J.C., 2006. Upper mantle *P*-wave speed variations beneath Ethiopia and the origin of the Afar hotspot. Geology 34, 329–332.
Bijwaard, H., Spakman, W., Engdahl, E.R., 1998. Closing the gap between regional and global travel time tomography. J. Geophys. Res. 103, 30,055–30,078.
Chang, S.-J., Van der Lee, S., Flanagan, M.P., Bedle, H., Marone, F., Matzel, E.M., Pasyanos, M.E., Rodgers, A.J., Romanowicz, B., Schmid, C., 2010. Joint inversion for 3-dimenstional S-velocity mantle structure along the Tethyan margin. J. Geophys. Res. 115, B08309. http://dx.doi.org/10.1029/2009JB007204.
Engdahl, E.R., Van der Hilst, R.D., Buland, R., 1998. Global teleseismic earthquake relocation with improved travel times and procedures for depth determination. Bull. Seism. Soc. Am. 88, 722–743.
Flanagan, M.P., Myers, S.C., Koper, K.D., 2007. Regional travel-time uncertainty and seismic location improvement using a three-dimensional a priori velocity model. Bull. Seism. Soc. Am. 97, 804–825.
Kennett, B.L.N., Engdahl, E.R., 1991. Traveltimes for global earthquake location and phase identification. Geophys. J. Int. 105, 429–465.
Koulakov, I., Kaban, M.K., Tesauro, M., Cloetingh, S., 2009. *P*- and *S*-velocity anomalies in the upper mantle beneath Europe from tomographic inversion of ISC data. Geophys. J. Int. 179, 345–366.
Marone, F., Van der Lee, S., Giardini, D., 2004. Three-dimensional upper-mantle *S*-velocity model for the Eurasia-Africa plate boundary region. Geophys. J. Int. 158, 109–130.
Montelli, R., Nolet, G., Dahlen, F.A., Masters, G., Engdahl, E.R., Hung, S.-H., 2004. Finite-frequency tomography reveals a variety of plumes in the mantle. Science 303, 338–343.
Paige, C.C., Saunders, M.A., 1982a. LSQR: an algorithm for sparse linear equations and sparse least squares. ACM Trans. Math. Softw. 8, 43–71.
Paige, C.C., Saunders, M.A., 1982b. LSQR: sparse linear equations and least squares problems. ACM Trans. Math. Softw. 8, 195–209.
Park, Y., Nyblade, A.A., 2006. *P*-wave tomography reveals a westward dipping low velocity zone beneath the Kenya Rift. Geophys. Res. Lett. 33, L07311. http://dx.doi.org/10.1029/2005GL025605.
Park, Y., Nyblade, A.A., Rodgers, A.J., Al-Amri, A., 2007. Upper mantle structure beneath the Arabian Peninsula and northern Red Sea from teleseismic body wave tomography: implication for the origin of Cenozoic uplift and volcanism in the Arabian Shield. Geochem. Geophys. Geosyst. 8, Q06021. http://dx.doi.org/10.1029/2006GC001566.
Rawlinson, N., Fishwick, S., in press. Seismic structure of the southeast Australian lithosphere from surface and body wave tomography. Tectonophysics doi: 10.1016/j.tecto.2011.11.016.
Ritzwoller, M.H., Shapiro, N.M., Levshin, A., Bergman, E.A., Engdahl, E.R., 2003. The ability of a global three-dimensional model to locate regional events. J. Geophys. Res. 108, 2353. http://dx.doi.org/10.1029/2002JB002167.
Schmid, C., Van der Lee, S., Giardini, D., 2004. Delay times and shear wave splitting in the Mediterranean region. Geophys. J. Int. 159, 275–290.
Simmons, N.A., Myers, S.C., Johannesson, G., 2011. Global-scale *P* wave tomography optimized for prediction of teleseismic and regional travel times for Middle East events: 2. Tomographic inversion. J. Geophys. Res. 116, B04305. http://dx.doi.org/10.1029/2010JB007969.
Spakman, W., Wortel, M.J.R., Vlaar, N.J., 1988. The Hellenic subduction zone: a tomographic image and its geodynamic implications. Geophys. Res. Lett. 15, 60–63.
Van der Hilst, R.D., Widiyantoro, S., Engdahl, E.R., 1997. Evidence for deep mantle circulation from global tomography. Nature 386, 578–584.
VanDecar, J.C., 1991. Upper-mantle structure of the Cascadia subduction zone from non-linear teleseismic travel-time inversion, Ph.D. thesis. University of Washington, Seattle.
VanDecar, J.C., Crosson, R.S., 1990. Determination of teleseismic relative phase arrival times using multi-channel cross-correlation and least-squares. Bull. Seism. Soc. Am. 80, 150–169.
Wang, Z., Dahlen, F.A., 1995. Spherical-spline parameterization of three-dimensional Earth models. Geophys. Res. Lett. 22, 3099–3102.
Wessel, P., Smith, W.H.F., 1998. New, improved version of the Generic Mapping Tools released. EOS Trans. AGU 79, 579.
Yang, T., Shen, Y., Van der Lee, S., Solomon, S.C., Hung, S.-H., 2006. Upper mantle structure beneath the Azores hotspot from finite-frequency seismic tomography. Earth Planet. Sci. Lett. 250, 11–26.